01 Nov 2023

Fabrication Process Independent And Robust Aggregation Of Detonation Nanodiamonds In Aqueous Media

Inga C. Kuschnerus

Haotian Wen

Xinrui Zeng

Yee Yee Khine

et. al. For a complete list of authors, see https://scholarsmine.mst.edu/chem_facwork/3643

Recommended Citation

I. C. Kuschnerus and H. Wen and X. Zeng and Y. Y. Khine and J. Ruan and C. J. Su and U. S. Jeng and H. A. Girard and J. C. Arnault and E. Ōsawa and O. Shenderova and V. Mochalin and M. Liu and M. Nishikawa, "Fabrication Process Independent And Robust Aggregation Of Detonation Nanodiamonds In Aqueous Media," *Diamond and Related Materials*, vol. 139, article no. 110199, Elsevier, Nov 2023.
The definitive version is available at https://doi.org/10.1016/j.diamond.2023.110199

Diamond & Related Materials 139 (2023) 110199

Contents lists available at ScienceDirect

Diamond & Related Materials

journal homepage: www.elsevier.com/locate/diamond

Fabrication process independent and robust aggregation of detonation nanodiamonds in aqueous media

Inga C. Kuschnerus [a,b], Haotian Wen [b], Xinrui Zeng [b], Yee Yee Khine [b], Juanfang Ruan [a], Chun-Jen Su [c], U-Ser Jeng [c,d], Hugues A. Girard [e], Jean-Charles Arnault [e], Eiji Ōsawa [f], Olga Shenderova [g], Vadym N. Mochalin [h,i], Ming Liu [j], Masahiro Nishikawa [j], Shery L.Y. Chang [a,b,*]

[a] Electron Microscope Unit, Mark Wainwright Analytical Centre, University of New South Wales, Sydney, Australia
[b] School of Materials Science and Engineering, University of New South Wales, Sydney, Australia
[c] National Synchrotron Radiation Research Center, Hsinchu Science Park, Hsinchu, Taiwan
[d] Department of Chemical Engineering, National Tsing Hua University, Hsinchu, Taiwan
[e] Université Paris-Saclay, CEA, CNRS, NIMBE, 91191 Gif sur Yvette, France
[f] NanoCarbon Research Institute, Ueda, Japan
[g] Adamas Nanotechnologies, Raleigh, USA
[h] Department of Chemistry, Missouri University of Science and Technology, Rolla, USA
[i] Department of Materials Science and Engineering, Missouri University of Science and Technology, Rolla, USA
[j] Daicel Corporation, Osaka, Japan

ARTICLE INFO

Keywords:
Nanodiamonds
Cryo-TEM
Machine learning
SAXS

ABSTRACT

In the past detonation nanodiamonds (DNDs), sized 3–5 nm, have been praised for their colloidal stability in aqueous media, thereby attracting vast interest in a wide range of applications including nanomedicine. More recent studies have challenged the consensus that DNDs are monodispersed after their fabrication process, with their aggregate formation dynamics poorly understood. Here we reveal that DNDs in aqueous solution, regardless of their post-synthesis de-agglomeration and purification methods, exhibit hierarchical aggregation structures consisting of chain-like and cluster aggregate morphologies. With a novel characterization approach combining machine learning with direct cryo-transmission electron microscopy and with X-ray scattering and vibrational spectroscopy, we show that their aggregate morphologies of chain and cluster ratios and the corresponding size and fractal dimension distributions vary with the post-synthesis treatment methods. In particular DNDs with positive ζ-potential form to a hierarchical structure that assembles aggregates into large networks. DNDs purified with the gas phase annealing and oxidation tend to have more chain-like aggregates. Our findings provide important contribution in understanding the DND interparticle interactions to control the size, polydispersity and aggregation of DNDs for their desired applications.

1. Introduction

Detonation nanodiamonds (DNDs) have been associated with a wide range of applications [1,2], for instance, drug delivery [3–9], gene therapy [10–12], as biomarkers in bioimaging [13–15], tissue engineering and bone surgery [16–19], photonic [20,21], spintronic [22] and as nanocomposites [23–26]. For any of these high-performance technologies, it is essential to control DND size, aggregation and polydispersity. For instance, in drug delivery, on the one hand, efficient compound loading relies on monodispersed particle to maximize the available surface area, while on the other hand, drug release can be slowed down (which is often desired) via the formation of robust porous microstructures [7,27,28].

In general, primary DNDs which are usually 3–5 nm in size tend to form larger aggregates during the cooling phase of the detonation process [29]. After detonation the DNDs are further treated with a range of post-synthesis techniques (as part of the fabrication process), which include processes for de-agglomeration and purification of DNDs for the

* Corresponding author at: Electron Microscope Unit, Mark Wainwright Analytical Centre, University of New South Wales, Sydney, Australia.
E-mail address: shery.chang@unsw.edu.au (S.L.Y. Chang).

https://doi.org/10.1016/j.diamond.2023.110199
Received 17 September 2022; Received in revised form 4 July 2023; Accepted 11 July 2023
Available online 22 July 2023

remaining and undesired non-sp^3 species in order to produce single-digit nanodiamonds. General approaches to tackle the persistent aggregation in DNDs are beads-assisted milling [29], oxidation through chemical treatment or annealing [2,30,31], and salt-assisted ultrasonic de-aggregation [32].

After the de-aggregation process DNDs are commonly labelled as monodispersed in solution, [33,34] usually confirmed by scattering techniques such as dynamic light scattering (DLS) and small angle X-ray scattering (SAXS). However, these characterization methods hold certain limitations. For instance, DLS only shows reliable size distributions for (quasi)-spherical particles. The size distributions observable in SAXS are limited to approximately a couple of 100 nm (depending on the scattering length density) by the scattering angle. By combining these conventional scattering techniques with additional characterization and analysis methods, more recent reports have challenged the assumption of monodispersed, de-aggregated DND [1,35–38]. Namely, Kuznetsow et al. showed in [36] that DNDs form chains in hydrosols, similar to the lacy networks formed by DNDs in water reported by Chang et al. in [37]. Kowalczyk et al. [1] found that even dried DND powders exhibit branched networks.

Due to these findings about the persistence of DND aggregates, controversy about the fabrication process of DNDs and their effectiveness in preventing agglomeration emerged. For instance, Knizhnik et al. [39] proposed a difference in the structural organization of DNDs with different ζ-potentials in water. Their work used cryo-transmission electron microscopy (cryo-TEM) to show that positively charged (hydrogen treated) DNDs form chains while negatively charged (oxygen-treated) DNDs form clusters. Their work proposes that the formation of chains from H-terminated DNDs is caused by charge separation followed by linking of DND particles due to electrostatic attraction of diamond facets with opposite charges. Further, bead assisted milling has been associated with a high amount of sp^2 carbon formation on the surface of DND particles, leading to the screening of facet-to-facet electrostatic interactions [36,40]. This implies that the higher fractions of sp^2 carbon present in DND (i.e. more graphitization on the surface) should promote the formation of clusters in DNDs [36]. Also, the type of purification treatment during DND processing has been speculated to influence aggregation [41]. DNDs have usually been treated by either wet or dry chemical purification. Even though the former using acid treatment has widely been employed, it has several limitations, i.e., it is less cost effective and environmentally friendly [30]. Instead of providing DNDs with sufficient purity, it may even induce higher chance of aggregation. Similarly, some of the dry purification methods, for example catalyst-assisted oxidation, oxidation using boric anhydride as an inhibitor of diamond oxidation, require either toxic and aggressive substances or supplementary catalysts, which also results in additional contamination or a significant loss of diamond phase [42]. Interaction of the DND surface with the surrounding medium has also been shown to have effects on the aggregation. Petit et al. [43] showed a long-range formation of the water hydrogen-bond network associated with hydrogenated surface groups in DNDs. Water hydrogen bond network was found to be different in aqueous dispersion of hydrogenated DNDs compared to DNDs terminated with other surface groups, which could be the consequence of an electron accumulation at the hydrogenated diamond–-water interface.

In addition to characterization and fabrication of DNDs, the driving force behind aggregate formation has been a topic of discussion [44–46]. First thought to be held together via random van der Waals-type inter-particle interactions, this hypothesis was put in question when experiments showed that DNDs are not dispersible using sonication [45,46]. Barnard et al. [46] attributed their formation to a mixture of coherent and incoherent interfacial Coulombic interactions (CICI and ICCI, respectively). The former gives rise to the ordered superstructure such as chains and loops due to the unisotropic, shape dependent surface electrostatic potential distributions and the latter gives random cluster aggregates. The coexistence of CICI and ICCI of DNDs has been confirmed by Chang et al. [38] using high-resolution transmission electron microscopy (HRTEM) on dried DND powder. Other studies mentioned the Derjaguin-Landau-Verwey-Overbeek (DLVO) theory to explain aggregation behavior, when interaction is due to van der Waals forces and repulsion by electrostatic interactions. However, this theory cannot fully explain the chain formation since it only considers simplified isotropic charge distribution (or simplified multi-poles). [39,47–49] More recent studies using course-grained molecular dynamics simulations of nanodiamond assembly have shown that the mechanism of the coexistence of the larger primary particles with dominating positively or negatively charged surface electrostatic potential form chain morphologies first and become the backbones of ropes and cluster assembly, which are formed by attaching the smaller and near-neutral particles to the backbones. The dispersion stabilizes eventually due the near-neutral particles coating the surface aggregates, preventing further aggregation and flocculation, which explains the long-term colloidal stability of DND-aggregates [50–52].

Considering the current controversy debates, there is a great need for more specialized characterization techniques to analyze the colloidal behavior of DNDs. Here we report direct, quantitative and statistical analysis of the DND aggregates in water, systematically over six types of purified samples obtained from different fabrication processes. Cryo-TEM, unlike conventional TEM, holds the advantages of imaging the particle suspension including gold, metal oxide, metal hydrite, micells, frozen in its native state [53,54], hence providing information about the dynamic formation process at high spatial resolution. Cryo-TEM has been previously used for DND characterization [36,37,39], however, only as supporting evidence, not providing sufficient statistics to be directly comparable with the bulk sample analysis such as DLS and SAXS.

Here, we use a newly developed quantitative, machine learning (ML) based cryo-TEM image analysis approach [50] to quantitatively and statistically analyze the DND aggregate morphology distributions in order to gain more understanding and statistics about the ensemble behavior of DNDs in solution. To address the debates about aggregation depending on differences in DND fabrication, six types of purified DND suspensions in water have been analyzed (wet chemistry vs. dry chemistry purification, beads-assisted milling vs. non-beads-assisted milling as de-agglomeration and positive vs. negative ζ-potential). Based on our systematic and statistical analysis of the experimental results, we show that the DND suspensions in water exhibit strong and robust aggregates consisting of ropes and clusters with distributions that are largely independent of their post-synthesis de-agglomeration process. Moreover, DNDs purified through gas phase methods tend to have more chain-like aggregates.

2. Experimental

2.1. Detonation nanodiamonds

The different DND suspensions were supplied by NanoCarbon Research Institute Ltd. (sample DND1-pos.), Daicel Corporation (sample DND2-pos. and sample DND3-neg.), one produced in-house (sample DND4-UD90-SAUD) and two supplied by Adamas Nanotechnologies (sample DND5-UD90 and DND6-UD90-pellet). The choice of purified DND suspensions covers the comparison of wet chemistry vs. dry chemistry as purification method (DND1-pos. vs. DND2-pos.), positive vs. negative ζ-potential (DND2-pos. vs. DND3-neg.) and beads-assisted milling vs. non beads-assisted milling as de-aggregation method (DND4-UD90-SAUD vs. DND5-UD90). DND5-UD90 and DND6-UD90-pellet were compared as control, since they are from the same bulk sample, however, DND6-UD90-pellet consists of the sediments of DND5-UD90 and therefore should contain mostly larger aggregates (see Table 1). Detailed fabrication process of these 6 nanodiamond can be found in the Supplementary Information.

Table 1
DND suspensions used for systematic comparison and the details of their fabrication methods.

Sample	Crude source	Purification method	De-aggregation method	ζ-potential (mV)
DND1-pos.[a]	NanoCarbon Research Institute Ltd.	Acid treatment	Beads-assisted milling	48.8 ± 4.9
DND2-pos.[a]	Daicel Corp.	Gas phase annealing	Beads-assisted milling	32.2 ± 1.8
DND3-neg.[a]	Daicel Corp.	Gas phase oxidation	Beads-assisted milling	−40.3 ± 3.0
DND4-UD90-SAUD	UD90	Gas phase oxidation [6]	Salt-assisted	−35.0 [32]
DND5-UD90[a]	UD90	Liquid phase oxidation [55]	Beads-assisted milling	−45.7 ± 1.6
DND6-UD90-pellet[a]	UD90	Liquid phase oxidation [55]	N/A (aggr.)	−26.5 ± 9.4

[a] Commercial samples.

2.2. Characterization methods

2.2.1. Cryo-TEM

The DND samples were prepared via freeze-plunging method for cryo-TEM imaging. The process of rapid cooling transforms (within microseconds) water into vitreous ice, thereby preserving the native state of the DND aggregates in solution. Approximately 1 wt% of each sample in deionized water were sonicated for ca. 30 min prior to being prepared for cryo-TEM. Afterwards, 4.5 μL of sample was deposited as a droplet onto the glow-discharged grid (R2/2 Quantifoil copper grids, Jena, Germany) using a Leica grid plunger at 15 °C, 89 % humidity and a blotting time of 3.5 s. Images were acquired using a Talos Artica TEM (Thermo Fisher Scientific, Waltham, USA) with an acceleration voltage of 200 keV.

2.2.2. Small angle X-ray scattering

SAXS data was collected using the TPS 13A BioSAXS beamline of the Taiwan Photon Source (TPS) at the National Synchrotron Radiation Research Center (NSRRC), Hsinchu [56]. With a 10 keV beam and a sample-to-detector distance of 5.32 m, the SAXS data were collected at a sample temperature of 318 K using the Eiger X 9M pixel detector in vacuum. The measured SAXS patterns were circularly averaged into 1D intensity distribution function $I(q)$, with the scattering vector $q = 4\pi\lambda^{-1}sin(\theta)$ defined by the scattering angle 2θ and X-ray wavelength λ. Data were corrected for transmission, background scattering, and pixel sensitivity of the detector, then scaled to the absolute intensity in units of cm^{-1} via comparing to the scattering intensity of water.

The DND samples studied here consist of primary particles which self-assemble into aggregates that in some cases form larger networks. Thus, a hierarchical structure, consisting of several characteristic length scales, is created which can be described by the concept of fractals. The primary particles can be modeled by spheres with a rough surface, represented by the so-called surface fractal dimension d_s [57]. The Beaucage model proposed a unified Guinier/power-law method which has proven to be a very appropriate tool to characterize multilevel structures. For an arbitrary number N of structural levels it can be written as [58]:

$$I = \sum_{i=1}^{N}\left[G_i exp\left(-q^2R_{g_i}^2/3\right) + B_i exp\left(-q^2R_{g_{i-1}}^2/3\right)\widetilde{q}^{P_i}\right] \quad (1)$$

with $\widetilde{q} = \left(erf\left(qR_{g_i}/6^{(1/2)}\right)\right)^3/q$. $i = 1$ refers to the smallest structural level, i.e., $R_{g_1} = r_g$ and $R_{g_2} = R_g$ are the radius of gyration of the primary particles and the aggregates, respectively. P_i refers to the slopes with $p_1 = (6 - d_s)$ and $d_f = p_2$. G_i is the Guinier prefactor and B_i is a scaling prefactor of the i-th level structure. More information on the theory can be found in the Supporting Information.

2.2.3. Vibrational spectroscopy

Approximately 10 μL of each nanodiamond dispersion was placed on a clean diamond ATR crystal and allowed to air dry in a desiccator for at least 1 h. Infrared spectroscopy was conducted using a Bruker Vertex80v FTIR spectrometer (Billerica, USA), equipped with a diamond ATR crystal. A background was taken prior to analysis of the dried dispersions and the ATR crystal was cleaned with ethanol prior to each analysis. All analyses were conducted under vacuum, with 128 scans collected over the region of 4000–400 cm^{-1}.

2.2.4. HRTEM and EELS

Aberration-corrected TEM imaging was performed using the JEM-ARM300F2 (Jeol Ltd., Tokyo, Japan) operated at 60 kV with a spatial resolution of 1 Å. Electron energy loss spectroscopy (EELS) was performed using Gatan GIF Continuum (Pleasanton, USA) with a dispersion of 30 meV per channel. The TEM specimens of all DND suspensions were prepared via drop-casting a diluted DND suspension onto holey carbon film coated Cu TEM grids and dried in vacuum for 5 min. In the case of EELS, samples were dried at 100 °C for 8 h.

2.3. Machine learning based quantitative image analysis of aggregate morphologies

In order to gain quantitative and statistical information of the aggregate morphology distribution, as well as their corresponding aggregate size and fractal dimension distributions, cryo-TEM images of all DND samples were processed and analyzed using our newly developed ML image process approach. Details of this method are described in ref. [50]. Briefly, the ML based image analysis method is divided into three parts: the first part is image pre-processing to identify the nanodiamond aggregates, by converting the raw cryo-TEM image intensity into binary data so that the background is separated from the aggregates. The second part is to apply the binary datasets for aggregate morphology labelling and categorizing into shape groups. The final part is the evaluation of the classified results and obtaining the relevant aggregate information including size distribution and fractal dimension.

In the first part, the image is pre-processed using a combination of automated dynamic thresholding, size thresholding, erosion-dilation and hole-filling methods to give accurate identification of DND particles and aggregates, and then the pre-processed images were converted to binary image datasets. In the second part, the converted image was processed by the in-house developed machine learning method that uses the hierarchical agglomerative clustering with the average linkage [59] for classification of aggregate morphologies, with pre-determined three aggregation shape groups. In the third step, the the resultant classified aggregate shapes were analyzed to extract the size distributions and their corresponding fractal dimensions. In the case of the chain and rope aggregates the size refers to their lengths, approximating the width of chains by the diameter of one nanodiamond (i.e. 5 nm), and that of ropes is taken to be equal to twice the diameter of a nanodiamond. The clusters are approximated to be disk shaped so the size is calculated as the diameter of the disk. The fractal dimension is determined using the Minkowski-Bouligand method [60].

For each sample >5 areas and >5 images, with approximately >20,000 DND particles, were analyzed.

3. Results and discussion

3.1. Cryo-TEM imaging revealing DND aggregate morphologies

Fig. 1a-f) shows the representative cryo-TEM images of the six

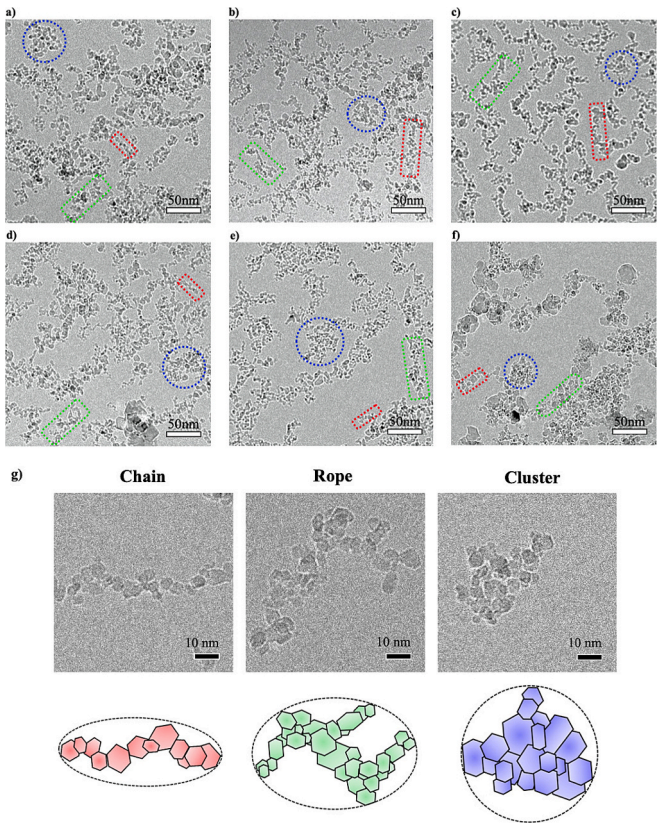

Fig. 1. Representative cryo-TEM images of all purified samples. a) Shows sample DND1-pos., b) DND2-pos., c) DND3-neg., d) DND4-UD90-SAUD, e) DND5-UD90, and f) DND6-UD90-pellet. Cluster is indicated by blue circle, ropes by green and chains by red shapes. g) Magnified images showing the representative chain, rope and cluster aggregate morphologies and their corresponding schematic illustrations.

purified DND samples described in Table 1, acquired under the same conditions. Upon visual examination, the images reveal that none of the samples is predominantly composed of mono-dispersed single particles. In fact, all samples exhibit three aggregate morphologies which we termed cluster, rope and chain, as indicated by the blue, green and red shapes in the figure. The chain refers to an ordered aggregate formed by connecting facets of individual DND particles, and has a nominal width of one particle. Ropes are similar to chains but they are wider and may have multiple branches. The cluster, shown in Fig. 1g), does not have any ordered inter-particle connections, and is composed of randomly connected DND particles.

Further inspection shows that all 6 samples have varying ratios of chain, rope and cluster morphologies. Samples DND1-pos. and DND2-pos. which both exhibit positive ζ-potential although with different purification methods (wet chemistry vs. dry chemistry purification), appear to have more interconnected aggregates, forming larger networks, compared to all others. In contrast, DND3-neg., a sample with different ζ-potential but same de-agglomeration method as DND2-pos., appears to have more chains and ropes with less clusters. Sample DND4-UD90-SAUD and DND5-UD90 prepared from the same source, are quite similar, although the former uses salt-assisted and the latter uses beads milling de-agglomeration methods. Interestingly, DND6-UD90-pellet consisting of the sediments of DND5-UD90, shows mostly cluster aggregates as expected, however, the rope morphology is still present.

3.2. Quantitative DND aggregate morphology distributions

In order to statistically assess the differences in the chain, rope and cluster ratios, a quantitative image analysis of all six samples (see Fig. 2) was performed using our in-house machine learning based image analysis method. To quantitatively compare images of the different samples without the influence of the concentration effects, it was ensured that the areal concentration of the DNDs (defined as the projected areas of DND over the total areas of the image) are the same (approximately 35 % for each sample). Fig. 2a-f) shows the same selected images as in Fig. 1a-f) after the quantitative analysis via ML algorithm.

Fig. 2g) confirms that all samples indeed exhibit a coexistence of chain, rope and cluster morphologies. Moreover, it reveals differences in the chain, rope and cluster ratios. All de-agglomerated samples (DND1–5) have about 50 % or higher combined ratio of chains and ropes, with DND samples purified by the gas phase annealing methods (DND2–3) showing higher combined ratios. Among the samples with positive ζ-potential but different purification methods, DND1-pos. (acid treatment) and DND2-pos. (gas phase annealing), DND1-pos. shows a very high number of clusters (55 %) and a lower number of ropes and chains (19.5 % and 24.9 %, respectively). In sample DND2-pos., the ratio of chains, clusters and ropes is more balanced, ranging between 26 and 29 %. Out of all six samples, DND3-neg. shows the highest number of ropes (39 %). The chain, rope and cluster ratios in DND4-UD90-SAUD and DND5-UD90 are very different from DND6-UD90-pellet. DND4-UD90-SAUD and DND5-UD90 exhibit almost similar amount of ropes, however, DND5-UD90 has a higher ratio of clusters. DND6-UD90-pellet

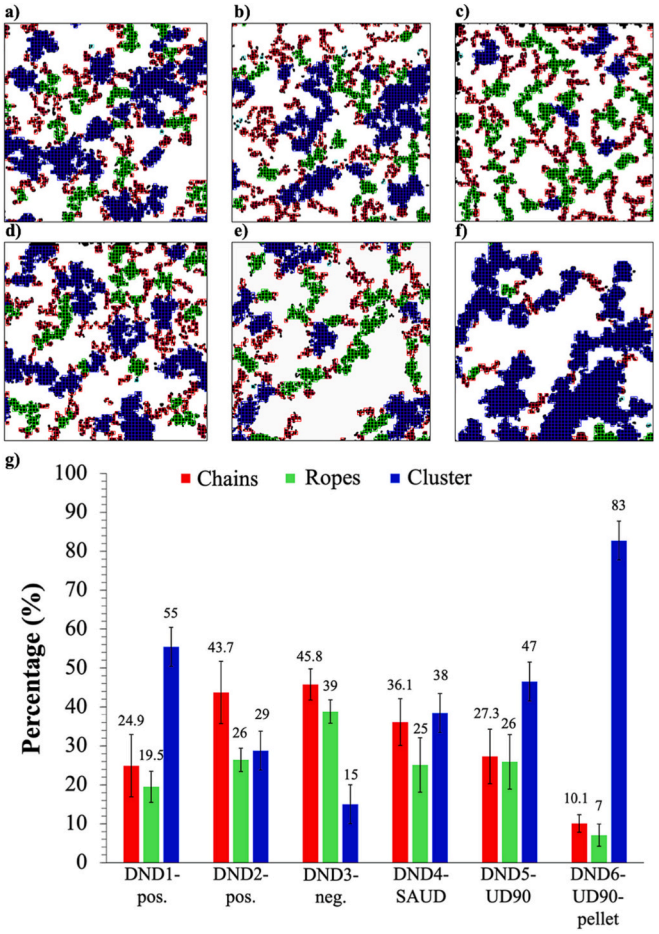

Fig. 2. Machine learning algorithm applied on cryo-TEM images of all purified samples showing classified morphologies indicated as chains (red), ropes (green) and clusters (blue). a) Shows sample DND1-pos., b) DND2-pos., c) DND3-neg., d) DND4-UD90-SAUD, e) DND5-UD90, and f) DND6-UD90-pellet. g) Quantitative analysis the fractions of each morphology. Error bars represent standard deviation of the mean value from analysis of different areas and images per sample.

contains highest cluster ratio of 83 %, as expected for the sediments of DND suspensions.

Additionally, the ML based analysis method is able to extract the size of each aggregate as well as the fractal dimension of individual clusters, giving the size and fractal dimension *distributions* rather than the averaged dimension as in SAXS. Fig. 3a-b) shows the size distributions for chains and ropes, respectively, and Fig. 3c) shows the scatter plot of the cluster diameter vs. the Minkowski-Bouligand fractal dimension.

It can be seen from Fig. 3a) that chain aggregates for all samples have highly skewed size distributions. They mostly range from 10 to 50 nm, and peak at around 12 nm. Two DND samples with positive ζ-potential (DND1–2) have small fractions of longer chains >150 nm. Similarly, rope aggregates also exhibit highly skewed distributions for all samples (Fig. 3b)), with most ropes size ranging from 25 to 75 nm, peaking at 25 nm. For cluster aggregates, it can be seen from Fig. 3c) that most cluster diameters range from 20 to 100 nm, concentrated around 20–40 nm. Their Minkowski-Bouligand fractal dimension is between 0.95 and 1.2, representing dendrite-like structures. Interestingly, DNDs with positive ζ-potential (DND1–2) have small fractions of clusters with larger cluster diameters and higher fractal dimensions (up to 1.5) which represent a"dragon curve" structure, a more interconnected, space filling structure compared to a dendrite structure. The DND pellet (DND6) shows a widest size range and high values of Minkowski-Bouligand dimension, indicating that larger and tighter clusters are present in the pellets.

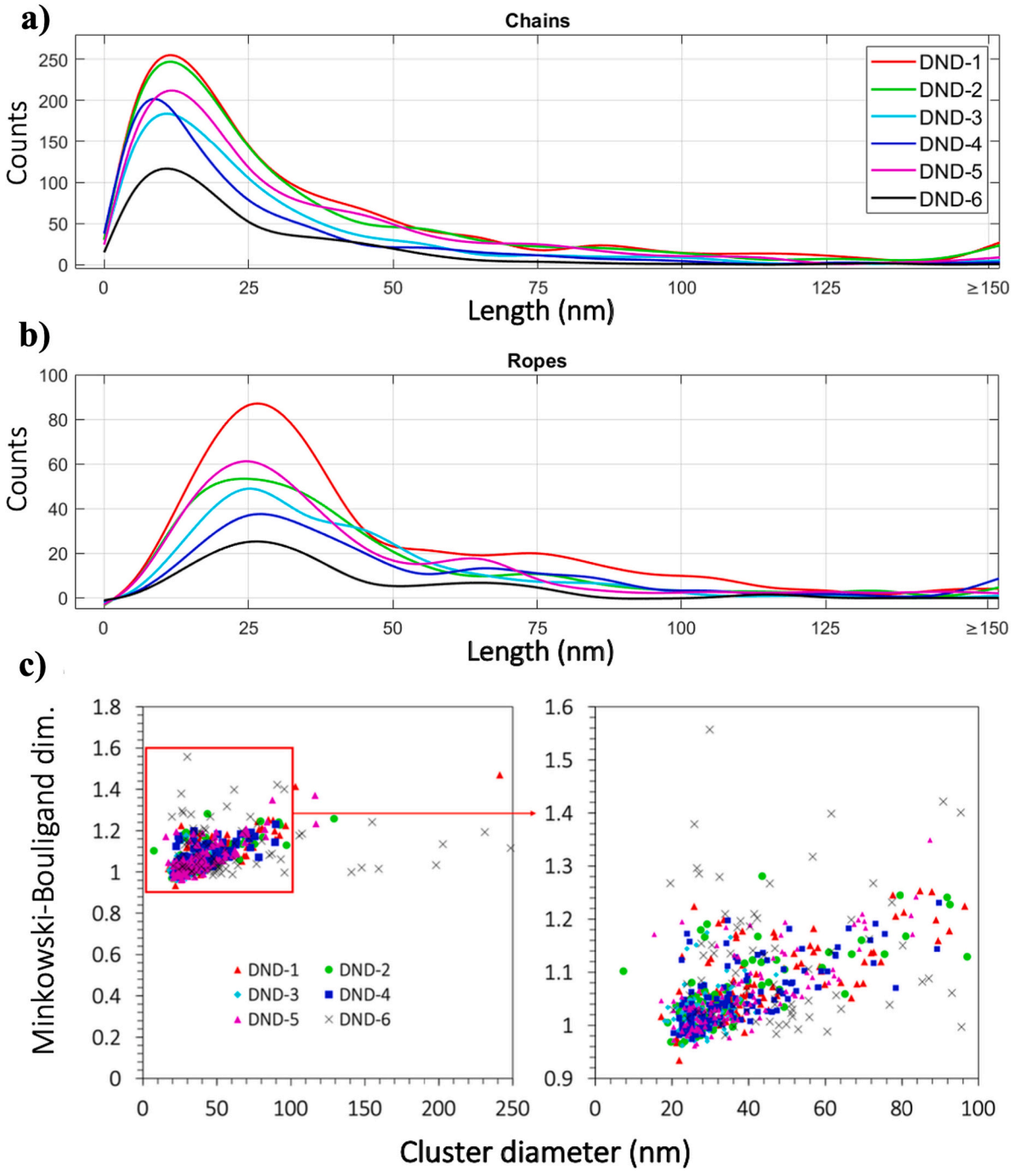

Fig. 3. a) Size histogram of chain aggregates; b) size histogram of rope aggregates; and c) scatter plot of Minkowski-Bouligand dimension with respect to cluster diameters for clusters.

The statistical and quantitative ML based image analysis reveals detailed differences among the DNDs with different fabrication and purification methods. Overall, we found that DNDs with positive ζ-potential tend to have longer chains and more interconnected clusters compared to those with negative ζ-potential. DNDs purified with gas phase annealing method (DND2–3) tend to have more chains and ropes and less clusters. There are no other apparent correlations with the post-synthesis de-agglomeration process.

3.3. DND aggregate size and shape analysis using SAXS

SAXS is one of the characterization methods used to derive complimentary information about the hierarchical structure of the primary particles forming aggregates which then assemble into networks. Fig. 4 shows the SAXS curves of all six purified samples. The intensity curves are normalized and multiplied by a constant factor to better visualize both differences and similarities. The circle symbols represent the experimental data, error bars are smaller than the symbol size and therefore omitted for the sake of clarity. In order to extract constitutive parameters, the curves were fitted by the unified model of Beaucage (see Eq. (1)) represented by the solid lines in Fig. 4. The dashed lines illustrate how the individual levels contribute to the full model.

Regardless of their ζ-potential or fabrication process, all curves show at least two different size populations (aggregates and primary particles), indicated by the two transitions in the scattering curve (e.g. $\mathbf{Rg}_{aggr}$ and $\mathbf{Rg}_p$), which is consistent with the SAXS data collected in [61]. Most of the curves look very similar, however, DND1-pos. and DND2-pos. are the only samples showing an upturn at a low q-range, indicating the presence of a third population, larger than $\mathbf{Rg}_{aggr.}$, e.g. networks. This is consistent with our results from the ML based image analysis that DND1-pos. and DND2-pos. have >150 nm longer chains and more interconnected clusters. Moreover, the curve for the sample DND6-UD90-pellet is the only one with a rather flat tail, with the radii of both populations ($\mathbf{Rg}_{aggr.}$ and $\mathbf{Rg}_p$) being very close to each other.

Table 2 shows the different radii for primary particles and aggregates derived from fitting the experimental data using the Beaucage model. The primary particle radii for the samples DND1 to DND5 range between 2.2 (DND4-UD90-SAUD) and 3.6 nm (DND2-pos.). DND6-UD90-pellet has a primary particle radius of 15 nm. This is most likely due to high amount of larger non-sp^3 carbon contaminants. The radii of the aggregates for all samples range between 30.9 and 46.2 nm. The size values of the primary particles and the aggregates are in good agreement to previous SAXS studies on DNDs, e.g., by Tomchuk et al. [63]. To quantitatively compare the SAXS measurement with our ML based image analysis, we also included the averaged value of the aggregate size for all three aggregate morphologies. This is calculated as the weighted average of the chain and rope lengths, and the cluster diameters. The weighting coefficient for each aggregate is their aggregate ratio, estimated from the ML classification, as shown in Fig. 2g). The error to the average aggregate size here indicates the large size distributions of the aggregates. In addition, we also include the average Minkowski–Bouligand fractal dimension calculated from all individual clusters. It should be noted here that the Minkowski–Bouligand fractal dimension is not the same as the Porod exponent that is typically used in the SAXS measurements. The aggregate size averaged through all three aggregate morphologies based on our method quantitatively, $\mathbf{R}_{ML}$, appears to be smaller than the aggregate size from SAXS measurements.

Table 2
DND average size and morphology analysis derived from SAXS and ML/cryo-TEM analysis. $\mathbf{Rg}_{aggr}$ refers to the radii of the aggregates and $\mathbf{Rg}_p$ to the radii of the primary particles analyzed using Beaucage model; $\mathbf{R}_{ML}$ refers to the weighted average size of clusters, ropes and chains in the sample. $\mathbf{FD}_m$ refers to Minkowski–Bouligand fractal dimensions.

Sample	$Rg_{aggr.}$ (nm)	Rg_p (nm)	R_{ML} (nm)	*FD_m
DND1	43.1	3.2	23.85 ± 12.45	1.08 ± 0.08
DND2	38.4	3.6	31.81 ± 15.47	1.06 ± 0.07
DND3	30.9	2.3	38.29 ± 18.75	1.03 ± 0.04
DND4	46.1	2.2	27.18 ± 14.48	1.05 ± 0.06
DND5	46.2	3.0	26.66 ± 20.08	1.07 ± 0.08
DND6	45.7	15.0	56.37 ± 20.73	1.12 ± 0.12

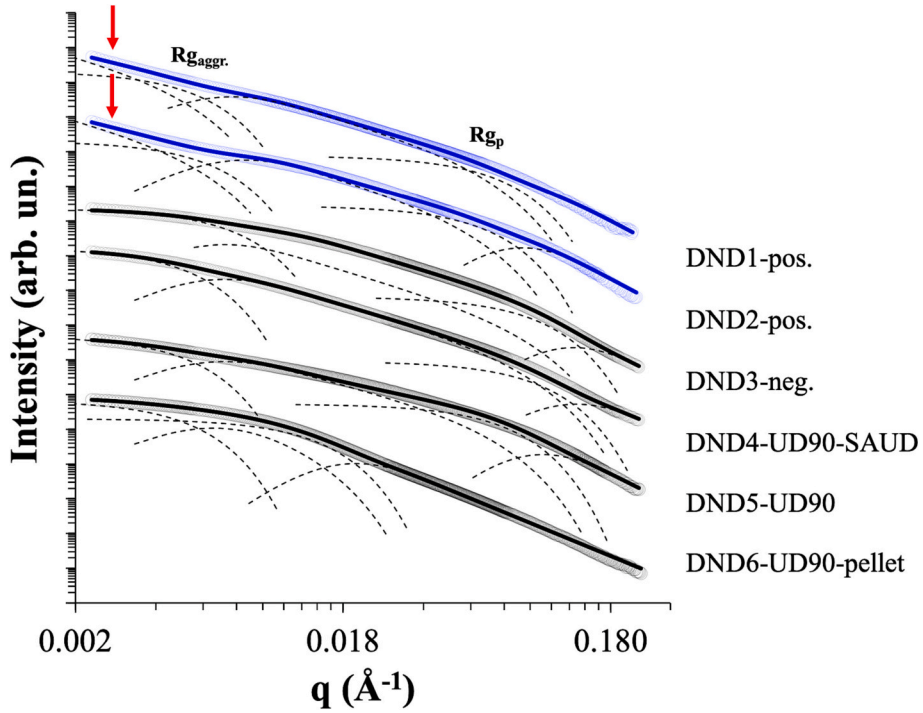

Fig. 4. Fitted SAXS curves derived from a unified Beaucage model of purified DND samples. The dashed lines illustrate how the individual levels contribute to the full model. Curves have been scaled for the sake of clarity. Blue spectra are samples with positive ζ-potential, black spectra represent samples with negative ζ-potential. Red arrows point towards upturn in the spectra indicating network formation.

The large standard variations reflect that the DNDs have rather skewed size distributions. Therefore an averaged estimate based on the ensemble measurement may not be adequate to reveal the complex dispersion behavior. Based on these comparisons, it is important to highlight that while SAXS is excellent for bulk analysis e.g. averaged aggregation behavior, the image based combined ML/cryo-TEM analysis method can provide additional complimentary and statistical information regarding the individual aggregate behavior. This information can be critical in understanding more complex and polydisperse systems. Overall, the combination of ML and cryo-TEM clearly holds an advantage in giving a more detailed description of all samples.

Using the Beaucage model to fit the data limits information access about the shape of the particles' aggregates, which are clearly visible in cryo-TEM. The more simplified Guinier-Porod model was additionally applied to the SAXS data (see Fig. S4 in the Supporting Information) to gather averaged information about the morphology of the aggregates. The extracted dimension variable **S** (presented in Table 1 in the Supporting Information) shows subtle differences between the samples. From sample DND1-pos. and DND2-pos. **S** values close to 2 indicate a plate-like morphology which can be interpreted as fractal networks [64]. This is again consistent with our ML based image analysis results.

3.4. Effect of surface chemistry on DND dispersion

Quantitative cryo-TEM imaging analysis, in agreement with SAXS results, suggests that there is no straightforward correlation with the aggregation morphology and the post-synthesis de-agglomeration process of DNDs. However, both characterization methods reveal that samples with positive ζ-potential (DND1-pos. and DND2-pos.) show the distinct hierarchical structure of primary particles forming aggregates which assemble into networks. The ζ-potential is affected by the surface chemistry of DNDs which in turn depends on the purification method during the fabrication process. In general, identifiable termination groups on DND surfaces include carboxyl groups, aldehydes, amines, hydroxyl and hydrogen, which are left over from the purification process [37,45,65].

The differences in the abundance of these groups influence the DND's ζ-potential (shown in Table 1). Fig. 5 displays the FTIR spectra of each purified sample. The spectra of the samples DND3 to DND6 are rich in carboxylic groups which show in a prominent peak at 1720–1740 cm^{-1}. DND1-pos. and DND2-pos. show distinct C—H stretching vibration and O—H stretching at approximately 2867 to 2981 cm^{-1} and 3200 to 3550 cm^{-1}. Electrostatic interactions between excess electrons at the water interface and CH_x groups from the DND surface would be expected and have been reported by Petit et al. in [43]. These long ranging attraction forces DNDs with positive ζ-potential to form networks (Table 3).

3.5. Effect of surface reconstruction/graphitization

As mentioned previously, bead-assisted milling has been associated with sp^2 carbon formation on the surface of DND particles, which has been hypothesized to screen electrostatic interactions [36,40]. This hypothesis has also been applied to explain the formation of nanopores in DND aggregates observed in water vapor adsorption measurements, [71] implying that the higher fractions of sp^2 carbon in DND (i.e. more graphitization on the surface) should promote formation of cluster morphologies. To establish if there is a correlation between the fraction of the sp^2 carbon and the DND aggregate morphology distributions, we have conducted sp^2/sp^3 ratio measurements using EELS. HRTEM imaging was also conducted to aid the interpretation of the origin of the sp^2 carbon, as amorphous, graphitic and DND surface reconstructed carbon can all give rise to π^* peak in EELS that is associated with sp^2 carbon. We

Table 3
Band assignments for FTIR spectra shown in Fig. 5.

No.	Range	Assignment	Functional class
1	920-950 1025-1035 1090-1140	C-O[a] [66,67]	Alcohols, phenols
2	1260–1290	C-O-C[a] [68,69]	Ethers
3	1325	C-H[b] [43,68]	Aldehydes
4	1440	OH[b] [43,69]	Carboxylic acids
5	1460–1480 1590–1660	C-H[b] [43,70]	Alkenes
6	1730–1757 1785–1810	C=O[a] [43] (H-bonded)	Carboxylic acids
7	2850–3000	CH_3, CH_2, CH[a] [43,68]	Alkanes
8	3200–3550	O-H[a] [43] (H-bonded)	Alcohols, phenols

[a] Stretching vibrations.
[b] Bending vibrations.

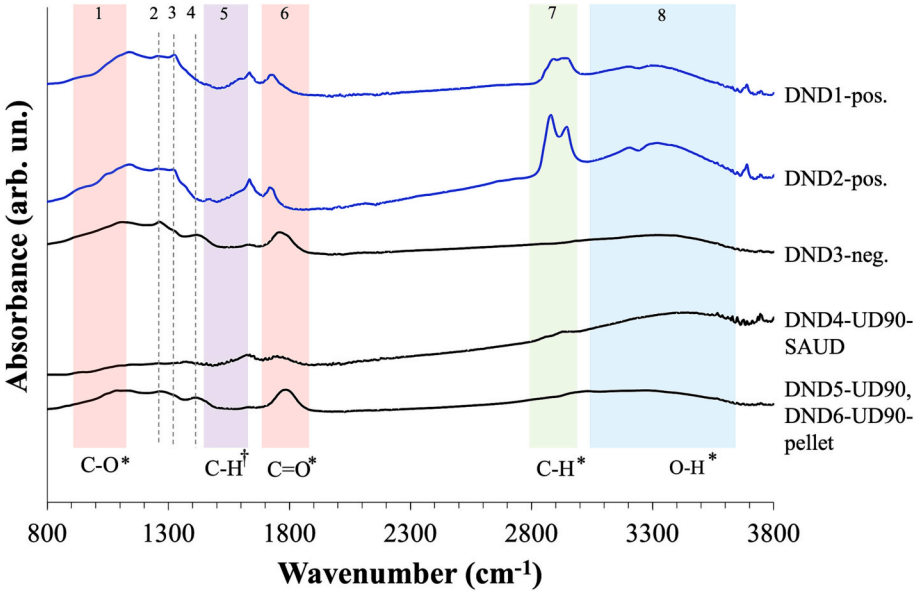

Fig. 5. FTIR results of purified samples. Blue spectra indicate samples with positive ζ-potential, black spectra indicate samples with negative ζ-potential. All spectra have been normalized and scaled for the sake of clarity. * indicates stretching vibrations; † bending vibrations.

note that XPS is not used here as the carbon contaminants in the DND suspensions may cause misinterpretation of the sp^2/sp^3 ratio. The HRTEM images in Fig. 6a-e) are representative for the samples investigated in this study and show the typical fullerene-like shell and crystalline diamond core of purified DNDs after de-aggregation. Such atomic structures are consistent with the electronic structure observations using EELS, where the C K-edge (Fig. 7b)) shows diamond-like edges with pronounced sp^3 peaks at ca. 289 eV. The near edge structure shows the presence of sp^2 and sp^{2+x} bonds characteristic of fullerene-like surface structure. EELS sp^2/sp^3 ratio analysis shows the surface graphitization average ranges between 28 and 36 % (DND2-pos. and DND6-UD90-pellet, respectively) (see Fig. 7). It appears that there are no significant differences in the sp^2 fraction among all samples. In particular, sample DND4-UD90-SAUD, the only sample that does not use bead-milling de-agglomeration process, does not show significantly reduced sp^2/sp^3 ratio, suggesting that the surface graphitization is not necessarily induced by the bead-assisted milling process. Therefore, we do not see a certain trend evolving by observation via EELS and HRTEM that explains the differences in the amount of cluster morphologies within the samples. It is also worth noting that the 28 and 36 % ratio we measured here is consistent with the first principle calculations of reconstructed 3–4 nm nanodiamond particles [72], in which the outmost surface layer is reconstructed to fullerence-like shell that accounts for about 30 % of sp^2 bonded carbon.

4. Conclusions

Using our newly developed particle aggregate characterization method by combining cryo-TEM imaging with machine learning approach, we were able to statistically measure the DND aqueous dispersion in their native state, giving the unambiguous information about the aggregate morphology and size distribution, as well as their fractal dimension distributions. Such information allows us to conclusively and systematically show that purified DND suspensions in water exhibit co-existence of chains, ropes and cluster structures in varying ratios, regardless of their fabrication process including wet chemistry vs. dry chemistry purification, bead-assisted milling vs. non-bead-assisted milling de-agglomeration and positive vs. negative ζ-potential. The strong and robust aggregates persist even in the sediments of DND suspensions.

The ratios between the three different morphologies, however, vary depending on the post-synthesis fabrication process. Quantitatively, we found that the lengths of chains and ropes for all samples mostly peaked at 12 and 25 nm. Only the samples with positive ζ-potential have small fractions of longer chains >150 nm. The size of cluster aggregates for most samples (except the pellet) concentrated around 20–40 nm, and their Minkowski-Bouligand fractal dimension is mostly between 0.95 and 1.2. The two samples with positive ζ-potential have small fractions of clusters extend to larger cluster diameters and higher fractal dimensions (up to 1.5).

While there are variations in aggregate morphology distributions and sizes among samples with different post-synthesis de-agglomeration process, two observable trends related to the purification process emerge from our comparisons. Firstly, the surface chemistry influences aggregate network formation above the size range of aggregates. Comparisons between the two samples with same deaggregation method but different signs of ζ-potential suggests that the DNDs with positive ζ-potential subject to a hierarchical structure of primary DNDs forming aggregates that assemble then into larger networks. This is confirmed through the ML based image analysis where significantly longer chains and more interconnected clusters were observed. SAXS measurement is also consistent with this image analysis result. Another trend is that DNDs purified through the gas phase annealing process tend to have more chains and ropes and less clusters.

Our findings unambiguously and systematically reveal the DND aggregation distribution in aqueous media. With the knowledge that the DND suspensions are not monodispersed, isolated single particles, but aggregates of chains, ropes and clusters, it should bring renewed understanding of their properties and applications. Hence, the results of this study provide pathways for controlling aggregate morphologies and polydispersity, which are critical for DND applications. The robustness of the aggregate formation against fabrication processes provides possibilities and flexibility of controlling aggregate morphologies and distributions tailored towards the needs of the desired applications.

CRediT authorship contribution statement

Inga C. Kuschnerus: Characterization, Data analysis, Investigation, Writing - original draft, Writing - review and editing. **Haotian Wen**: Investigation, Data analysis, Writing - review and editing. **Xinrui Zeng**: Investigation, Data analysis, Writing - review and editing. **Yee Yee Khine**: Investigation, Data analysis, Writing - review and editing.

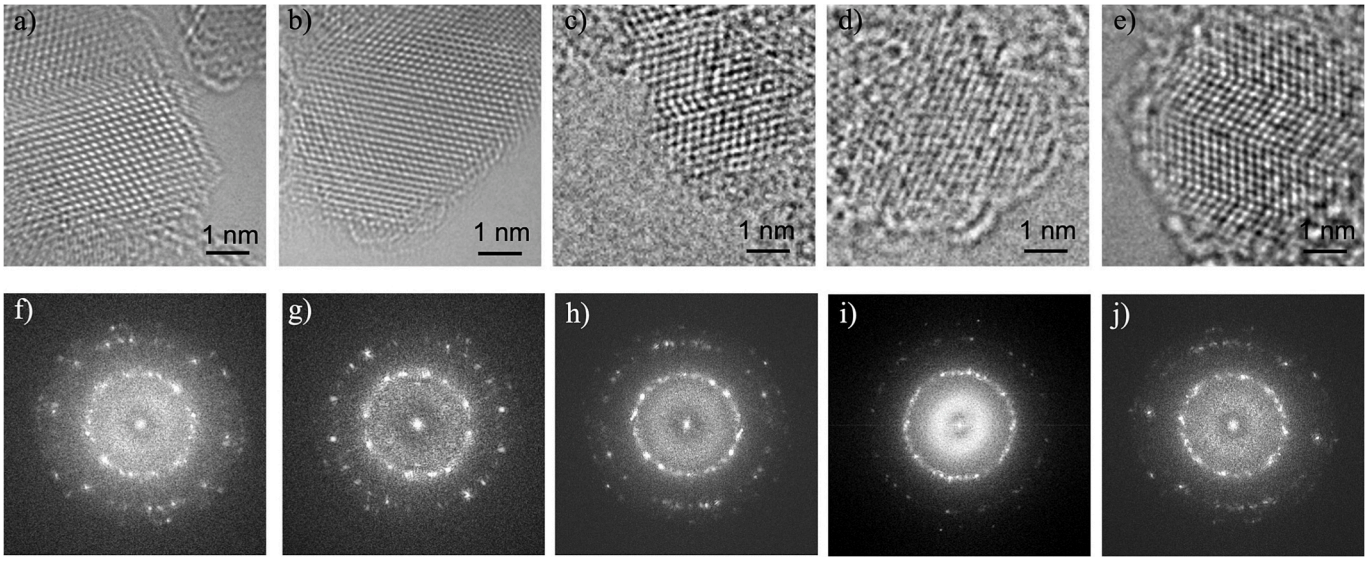

Fig. 6. a-e) HRTEM images of representative areas of samples DND1-pos., DND2-pos., DND3-neg., DND4-SAUD and DND5-UD90. All samples show crystalline diamond structured core and fullerene-like sp^2 and sp^{2+x} surface reconstructed shells. Images f-j) show the diffractograms of larger representative areas of each sample. There are no obvious differences in the crystalline structure of the samples. Note that DND6-UD90-pellet is omitted here as it is the pellet of DND5.

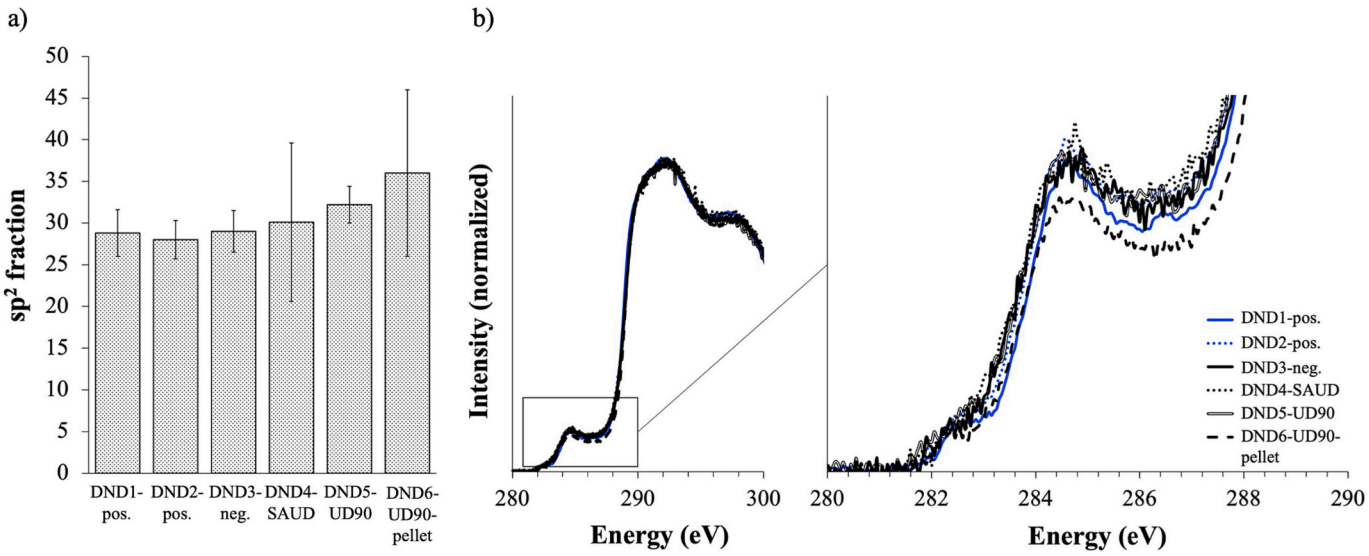

Fig. 7. a) Quantification of sp^2/sp^3 ratio for samples DND1-pos., DND2-pos., DND3-neg., DND4-SAUD and DND5-UD90. and DND6-UD90-pellet. The average and standard deviation are calculated based on the EELS spectra from 10 areas. Therefore, the error bars (standard deviations) reflect the degree of in-homogeneity in the sample. b) Averaged EELS spectra of the C—K edge. The electronic structure of the nanodiamond measured by EELS also confirms the fullerene-like nature of the nanodiamond surface.

Juanfang Ruan: Investigation, Characterization, Writing - review and editing. **Chun-Jen Su**: Characterization, Data analysis, Writing - review and editing. **U-Ser Jeng**: Data analysis, Writing - review and editing. **Eiji Ōsawa**: Investigation. **Olga Shenderova**: Investigation, Writing - review and editing. **Vadym Mochalin**: Investigation, Writing - review and editing. **Ming Liu**: Investigation, Writing - review and editing. **Masahiro Nishikawa**: Investigation. **Shery L. Y. Chang**: Conceptualization, Supervision, Characterization, Data analysis, Investigation, Writing - review and editing.

Declaration of competing interest

The authors declare that they have no known competing financial interests or personal relationships that could have appeared to influence the work reported in this paper.

Data availability

Data will be made available on request.

Acknowledgements

SLYC and ICK acknowledge the use of TEMs at the Electron Microscope Unit, Mark Wainwright Analytical Centre, UNSW. SLYC also acknowledge the use of vibrational spectroscopy facility at the University of Sydney. The authors acknowledge the SAXS data collection at NSRRC during COVID-19 pandemic. SLYC acknowledges the support by the Australian Research Council (ARC) under grant IC210100056. VNM acknowledges partial support from the National Eye Institute of the National Institutes of Health under Award Number 1R15EY029813-01A1.

Appendix A. Supplementary data

Supplementary data to this article can be found online at https://doi.org/10.1016/j.diamond.2023.110199.

References

[1] P. Kowalczyk, E.-Z. Piña-Salazar, J. Judas, A.P. Terzyk, R. Futamura, T. Hayashi, E. Ōsawa, K. Kaneko, A. Ciach, Reconstructing the fractal clusters of detonation nanodiamonds from small-angle X-ray scattering, Carbon 169 (2020) 349–356.
[2] V. Mochalin, O. Shenderova, D. Ho, Y. Gogotsi, The properties and applications of nanodiamonds, Nat. Nanotechnol. 7 (2012) 11–23.
[3] D. Ho, C.-H.K. Wang, E.K.-H. Chow, Nanodiamonds: the intersection of nanotechnology, drug development, and personalized medicine, Sci. Adv. 1 (7) (2015), e1500439.
[4] S. Chauhan, N. Jain, U. Nagaich, Nanodiamonds with powerful ability for drug delivery and biomedical applications: recent updates on in vivo study and patents, J. Pharm. Anal. 10 (1) (2020) 1–12.
[5] E. Perevedentseva, Y.-C. Lin, C.-L. Cheng, A review of recent advances in nanodiamond-mediated drug delivery in cancer, Expert Opin. Drug Deliv. 18 (3) (2021) 369–382.
[6] V.N. Mochalin, A. Pentecost, X.-M. Li, I. Neitzel, M. Nelson, C. Wei, T. He, F. Guo, Y. Gogotsi, Adsorption of drugs on nanodiamond: toward development of a drug delivery platform, Mol. Pharm. 10 (10) (2013) 3728–3735.
[7] J. Giammarco, V.N. Mochalin, J. Haeckel, Y. Gogotsi, The adsorption of tetracycline and vancomycin onto nanodiamond with controlled release, J. Colloid Interface Sci. 468 (2016) 253–261.
[8] J. Beltz, A. Pfaff, I.M. Abdullahi, A. Cristea, V.N. Mochalin, N. Ercal, Effect of nanodiamond surface chemistry on adsorption and release of tiopronin, Diam. Relat. Mater. 100 (2019), 107590.
[9] K. Turcheniuk, V.N. Mochalin, Biomedical applications of nanodiamond, Nanotechnology 28 (25) (2017), 252001.
[10] J.-R. Bertrand, C. Pioche-Durieu, J. Ayala, T. Petit, H.A. Girard, C.P. Malvy, E. Le Cam, F. Treussart, J.-C. Arnault, Plasma hydrogenated cationic detonation nanodiamonds efficiently deliver to human cells in culture functional sirna targeting the Ewing sarcoma junction oncogene, Biomaterials 45 (2015) 93–98.
[11] H.M. Leung, M.S. Chan, L.S. Liu, S.W. Wong, T.W. Lo, C.-H. Lau, C. Tin, P.K. Lo, Dual-function, cationic, peptide-coated nanodiamond systems: facilitating nuclear-targeting delivery for enhanced gene therapy applications, ACS Sustain. Chem. Eng. 6 (8) (2018) 9671–9681.
[12] X.-Q. Zhang, M. Chen, R. Lam, X. Xu, E. Ōsawa, D. Ho, Polymer-functionalized nanodiamond platforms as vehicles for gene delivery, ACS Nano 3 (9) (2009) 2609–2616.
[13] G. Hong, S. Diao, A.L. Antaris, H. Dai, Carbon nanomaterials for biological imaging and nanomedicinal therapy, Chem. Rev. 115 (19) (2015) 10816–10906.
[14] Y. Kuo, T.-Y. Hsu, Y.-C. Wu, H.-C. Chang, Fluorescent nanodiamond as a probe for the intercellular transport of proteins in vivo, Biomaterials 34 (33) (2013) 8352–8360.
[15] W. Hou, T.B. Toh, L.N. Abdullah, T.W.Z. Yvonne, K.J. Lee, I. Guenther, E.K.-H. Chow, Nanodiamond–manganese dual mode mri contrast agents for enhanced liver tumor detection, Nanomedicine 13 (3) (2017) 783–793.
[16] K. Fox, R. Ratwatte, M.A. Booth, H.M. Tran, P.A. Tran, High nanodiamond content-pcl composite for tissue engineering scaffolds, Nanomaterials 10 (5) (2020) 948.
[17] J. Nunes-Pereira, A. Silva, C. Ribeiro, S. Carabineiro, J. Buijnsters, S. Lanceros-Méndez, Nanodiamonds/poly(vinylidene fluoride) composites for tissue engineering applications, Compos. Part B 111 (2017) 37–44.

[18] Q. Zhang, V.N. Mochalin, I. Neitzel, I.Y. Knoke, J. Han, C.A. Klug, J.G. Zhou, P. I. Lelkes, Y. Gogotsi, Fluorescent plla-nanodiamond composites for bone tissue engineering, Biomaterials 32 (1) (2011) 87–94.

[19] Q. Zhang, V.N. Mochalin, I. Neitzel, K. Hazeli, J. Niu, A. Kontsos, J.G. Zhou, P. I. Lelkes, Y. Gogotsi, Mechanical properties and biomineralization of multifunctional nanodiamond-plla composites for bone tissue engineering, Biomaterials 33 (20) (2012) 5067–5075.

[20] V. Grichko, T. Tyler, V.I. Grishko, O. Shenderova, Nanodiamond particles forming photonic structures, Nanotechnology 19 (22) (2008), 225201.

[21] M. Radulaski, J.L. Zhang, Y.-K. Tzeng, K.G. Lagoudakis, H. Ishiwata, C. Dory, K. A. Fischer, Y.A. Kelaita, S. Sun, P.C. Maurer, K. Alassaad, G. Ferro, Z.-X. Shen, N. A. Melosh, S. Chu, J. Vučković, Nanodiamond integration with photonic devices, Laser Photonics Rev. 13 (8) (2019) 1800316.

[22] P.G. Baranov, I.V. Il'in, A.A. Soltamova, A.Y. Vul', S. Kidalov, F.M. Shakhov, G. V. Mamin, S.B. Orlinskii, M.K. Salakhov, Electron spin resonance detection and identification of nitrogen centers in nanodiamonds, J. Exp. Theor. Phys. Lett. 89 (2009) 409–413.

[23] Y. Zhang, K.Y. Rhee, D. Hui, S.-J. Park, A critical review of nanodiamond based nanocomposites: synthesis, properties and applications, Compos. Part B 143 (2018) 19–27.

[24] T. Subhani, M. Latif, I. Ahmad, S.A. Rakha, N. Ali, A.A. Khurram, Mechanical performance of epoxy matrix hybrid nanocomposites containing carbon nanotubes and nanodiamonds, Mater. Des. 87 (2015) 436–444.

[25] F. Zhang, T. Liu, Nanodiamonds reinforced titanium matrix nanocomposites with network architecture, Compos. Part B 165 (2019) 143–154.

[26] I. Neitzel, V.N. Mochalin, Y. Gogotsi, Chapter 14 - nanodiamonds in composites: polymer chemistry and tribology, in: Nanodiamonds, Micro and Nano Technologies, Elsevier, 2017, pp. 365–390.

[27] J. Liu, Y. Huang, A. Kumar, A. Tan, S. Jin, A. Mozhi, X.-J. Liang, ph-sensitive nano-systems for drug delivery in cancer therapy, Biotechnol. Adv. 32 (4) (2014) 693–710.

[28] Y. Liu, W. Wang, J. Yang, C. Zhou, J. Sun, ph-sensitive polymeric micelles triggered drug release for extracellular and intracellular drug targeting delivery, Asian J. Pharm. Sci. 8 (3) (2013) 159–167.

[29] A. Krüger, F. Kataoka, M. Ozawa, T. Fujino, Y. Suzuki, A.E. Aleksenskii, A.Y. Vul', E. Ōsawa, Unusually tight aggregation in detonation nanodiamond: identification and disintegration, Carbon 43 (8) (2005) 1722–1730.

[30] D.M. Gruen, O.A. Shenderova, A.Y. Vul, Synthesis, Properties and Applications of Ultrananocrystalline Diamond: Proceedings of the NATO ARW on Synthesis, Properties and Applications of Ultrananocrystalline Diamond, St. Petersburg, Russia, From 7 to 10 June 2004 Vol. 192, Springer Science & Business Media, 2005.

[31] O.A. Shenderova, V.V. Zhirnov, D.W. Brenner, Carbon nanostructures, Crit. Rev. Solid State Mater. Sci. 27 (2002) 227.

[32] K. Turcheniuk, C. Trecazzi, C. Deeleepojananan, V.N. Mochalin, Salt-assisted ultrasonic deaggregation of nanodiamond, ACS Appl. Mater. Interfaces 8 (38) (2016) 25461–25468.

[33] D. Terada, T.F. Segawa, A.I. Shames, S. Onoda, T. Ohshima, E. Ōsawa, R. Igarashi, M. Shirakawa, Monodisperse five-nanometer-sized detonation nanodiamonds enriched in nitrogen-vacancy centers, ACS Nano 13 (6) (2019) 6461–6468.

[34] E. Ōsawa, Monodisperse single nanodiamond particulates, Pure Appl. Chem. 80 (07 2008) 1365–1379.

[35] K. Katsiev, V. Solovyeva, R. Mahfouz, E. Abou-Hamad, W. Peng, H. Idriss, A. R. Kirmani, Fresh insights into detonation nanodiamond aggregation: an X-ray photoelectron spectroscopy, thermogravimetric analysis, and nuclear magnetic resonance study, Eng. Rep. 3 (3) (2021), e12375.

[36] N.M. Kuznetsov, S.I. Belousov, A.V. Bakirov, S.N. Chvalun, R.A. Kamyshinsky, A. A. Mikhutkin, A.L. Vasiliev, P.M. Tolstoy, A.S. Mazur, E.D. Eidelman, E.B. Yudina, A.Y. Vul, Unique rheological behavior of detonation nanodiamond hydrosols: the nature of sol-gel transition, Carbon 161 (2020) 486–494.

[37] S.L.Y. Chang, P. Reineck, D. Williams, G. Bryant, G. Opletal, S.A. El-Demrdash, P.-L. Chiu, E. Ōsawa, A.S. Barnard, C. Dwyer, Dynamic self-assembly of detonation nanodiamond in water, Nanoscale 12 (9) (2020) 5363–5367.

[38] L.-Y. Chang, E. Ōsawa, A.S. Barnard, Confirmation of the electrostatic self-assembly of nanodiamonds, Nanoscale 3 (2011) 958–962.

[39] A.A. Knizhnik, Y.G. Polynskaya, A.S. Sinitsa, N.M. Kuznetsov, S.I. Belousov, S. N. Chvalun, B.V. Potapkin, Analysis of structural organization and interaction mechanisms of detonation nanodiamond particles in hydrosols, Phys. Chem. Chem. Phys. 23 (2021) 674–682.

[40] A.Y. Vul', E.D. Eydelman, M. Inakuma, E. Ōsawa, Correlation between viscosity and absorption of electromagnetic waves in an aqueous uncd suspension, Diam. Relat. Mater. 16 (12) (2007) 2023–2028.

[41] V.Y. Dolmatov, Ultradisperse diamonds produced by detonation synthesis: properties and applications, Russ. Chem. Rev. 70 (2001) 607–626.

[42] S. Osswald, G. Yushin, V. Mochalin, S.O. Kucheyev, Y. Gogotsi, Control of sp2/sp3 carbon ratio and surface chemistry of nanodiamond powders by selective oxidation in air, J. Am. Chem. Soc. 128 (35) (2006) 11635–11642.

[43] T. Petit, L. Puskar, T. Dolenko, S. Choudhury, E. Ritter, S. Burikov, K. Laptinskiy, Q. Brzustowski, U. Schade, H. Yuzawa, M. Nagasaka, N. Kosugi, M. Kurzyp, A. Venerosy, H. Girard, J.-C. Arnault, E. Ōsawa, N. Nunn, O. Shenderova, E.F. Aziz, Unusual water hydrogen bond network around hydrogenated nanodiamonds, J. Phys. Chem. C 121 (9) (2017) 5185–5194.

[44] A. Pentecost, S. Gour, V. Mochalin, I. Knoke, Y. Gogotsi, Deaggregation of nanodiamond powders using salt- and sugar-assisted milling, ACS Appl. Mater. Interfaces 2 (11) (2010) 3289–3294.

[45] L. Lai, A.S. Barnard, Interparticle interactions and self-assembly of functionalized nanodiamonds, J. Phys. Chem. Lett. 3 (7) (2012) 896–901.

[46] A.S. Barnard, Self-assembly in nanodiamond agglutinates, J. Mater. Chem. 18 (2008) 4038–4041.

[47] N. Kuznetsov, S. Belousov, D. Stolyarova, A. Bakirov, S. Chvalun, A. Shvidchenko, E. Eidelman, A. Vul', Effect of diamond nanoparticle chains on rheological properties of hydrosol, Diam. Relat. Mater. 83 (2018) 141–145.

[48] A. Shvidchenko, E. Eidelman, A. Vul', N. Kuznetsov, D. Stolyarova, S. Belousov, S. Chvalun, Colloids of detonation nanodiamond particles for advanced applications, Adv. Colloid Interf. Sci. 268 (2019) 64–81.

[49] A. Vul, E. Eidelman, A. Aleksenskiy, A. Shvidchenko, A. Dideikin, V. Yuferev, V. Lebedev, Y. Kul'velis, M. Avdeev, Transition sol-gel in nanodiamond hydrosols, Carbon 114 (2017) 242–249.

[50] I.C. Kuschnerus, H. Wen, J. Ruan, X. Zeng, C.-J. Su, U.-S. Jeng, G. Opletal, A. S. Barnard, M. Liu, M. Nishikawa, S.L.Y. Chang, Complex dispersion of detonation nanodiamond revealed by machine learning assisted cryo-tem and coarse-grained molecular dynamics simulations, ACS Nanosci. Au 3 (3) (2023) 211–221.

[51] G. Opletal, A.S. Barnard, Simulating facet-dependent aggregation and assembly of mixtures of polyhedral nanoparticles, Adv. Theory Simul. 5 (2021) 2100279.

[52] G. Opletal, S.L.Y. Chang, A.S. Barnard, Simulating facet-dependent aggregation and assembly of distributions of polyhedral nanoparticles, Nanoscale 12 (2020) 19870.

[53] N.D. Burrows, R.L. Penn, Cryogenic transmission electron microscopy: aqueous suspensions of nanoscale objects, Microsc. Microanal. 19 (2013) 1.

[54] C.A. Monnier, D.C. Thévenaz, S. Balog, G.L. Fiore, D. Vanhecke, B. Rothen-Rutishauser, A. Petri-Fink, A guide to investigating colloidal nanoparticles by cryogenic transmission electron microscopy: pitfalls and benefits, AIMS Biophys. 2 (2015) 245.

[55] P. Reineck, D.W.M. Lau, E.R. Wilson, N. Nunn, O.A. Shenderova, B.C. Gibson, Visible to near-ir fluorescence from single-digit detonation nanodiamonds: excitation wavelength and ph dependence, Sci. Report. 8 (2478) (2018).

[56] O. Shih, K.-F. Liao, Y.-Q. Yeh, C.-J. Su, C.-A. Wang, J.-W. Chang, W.-R. Wu, C.-C. Liang, C.-Y. Lin, T.-H. Lee, C.-H. Chang, L.-C. Chiang, C.-F. Chang, D.-G. Liu, M.-H. Lee, C.-Y. Liu, T.-W. Hsu, B. Mansel, M.-C. Ho, C.-Y. Shu, F. Lee, E. Yen, T.-C. Lin, U. Jeng, Performance of the new biological small- and wide-angle X-ray scattering beamline 13A at the Taiwan Photon Source, J. Appl. Crystallogr. 55 (2022) 340–352.

[57] G.J. Schneider, V. Vollnhals, K. Brandt, S.V. Roth, D. Göritz, Correlation of mass fractal dimension and cluster size of silica in styrene butadiene rubber composites, J. Chem. Phys. 133 (9) (2010), 094902.

[58] G. Beaucage, Approximations leading to a unified exponential/power-law approach to small-angle scattering, J. Appl. Crystallogr. 28 (6) (1995) 717–728.

[59] A.K. Jain, Data clustering: 50 years beyond k-means, Pattern Recogn. Lett. 31 (8) (2010) 651–666.

[60] A. Napolitano, S. Ungania, V. Cannata, Fractal dimension estimation methods for biomedical images, in: MATLAB—A Fundamental Tool for Scientific Computing and Engineering Applications 3, 2012, pp. 161–178.

[61] N.M. Kuznetsov, A.Y. Vdovichenko, A.V. Bakirov, S.I. Belousov, R.A. Kamyshinsky, A.L. Vasiliev, E.S. Kulikova, R.D. Svetogorov, S.N. Chvalun, E.B. Yudina, A.Y. Vul', The size effect of faceted detonation nanodiamond particles on electrorheological behavior of suspensions in mineral oil, Diam. Relat. Mater. 125 (2022), 108967.

[63] O.V. Tomchuk, M.V. Avdeev, A.E. Aleksenskii, A.Y. Vul, O.I. Ivankov, V. V. Ryukhtin, J. Füzi, V.M. Garamus, L.A. Bulavin, Sol–gel transition in nanodiamond aqueous dispersions by small-angle scattering, J. Phys. Chem. C 123 (29) (2019) 18028–18036.

[64] S.A. El-Demrdash, R. Nixon-Luke, L. Thomsen, A. Tadich, D.W.M. Lau, S.L. Y. Chang, T.L. Greaves, G. Bryant, P. Reineck, The effect of salt and particle concentration on the dynamic self-assembly of detonation nanodiamonds in water, Nanoscale 13 (2021) 14110–14118.

[65] A. Kume, V.N. Mochalin, Sonication-assisted hydrolysis of ozone oxidized detonation nanodiamond, Diam. Relat. Mater. 103 (2020), 107705.

[66] B.J. Meldrum, C.H. Rochester, In situ infrared study of the surface oxidation of activated carbon in oxygen and carbon dioxide, J. Chem. Soc. Faraday Trans. 86 (1990) 861–865.

[67] C. Ávila Orta, V. Cruz-Delgado, M. Neira-Velázquez, E. Hernández-Hernández, M. Méndez-Padilla, F. Medellín-Rodríguez, Surface modification of carbon nanotubes with ethylene glycol plasma, Carbon 47 (8) (2009) 1916–1921.

[68] T. Jiang, K. Xu, Ftir study of ultradispersed diamond powder synthesized by explosive detonation, Carbon 33 (12) (1995) 1663–1671.

[69] L.M. Struck, M.P. D'Evelyn, Interaction of hydrogen and water with diamond (100): infrared spectroscopy, J. Vac. Sci. Technol. A 11 (4) (1993) 1992–1997.

[70] J.-S. Tu, E. Perevedentseva, P.-H. Chung, C.-L. Cheng, Size-dependent surface co stretching frequency investigations on nanodiamond particles, J. Chem. Phys. 125 (17) (2006), 174713.

[71] E.-Z. Pina-Salazar, K. Urita, T. Hayashi, R. Futamura, F. Vallejos-Burgos, J. WÅ, och, P. Kowalczyk, M. Wiśniewski, T. Sakai, I. Moriguchi, A.P. Terzyk, E. Ōsawa, K. Kaneko, Water adsorption property of hierarchically nanoporous detonation nanodiamonds, Langmuir 33 (42) (2017) 11180–11188.

[72] S.L.Y. Chang, C. Dwyer, E. Ōsawa, A.S. Barnard, Size dependent surface reconstruction in detonation nanodiamonds, Nanoscale Horiz. 3 (2018) 213–217.